

UNIVERSIDAD DE LOS ANDES



Phenomenological Study of Search of Heavy Neutrinos, with Displaced Vertices and Vector Boson Fusion

THIS DISSERTATION IS SUBMITTED FOR THE DEGREE OF

PHYSICIST

BY

SANDRA JIMENA GONZÁLEZ LOZANO

ADVISOR: ANDRÉS FLÓREZ

BOGOTÁ, D.C.

2017

Contents

1	Introduction	1
2	State of the Art	5
2.1	Standard Model	5
2.2	Neutrinos in the Standard Model	7
2.2.1	Dirac Mass	7
2.2.2	Majorana Mass	8
2.3	Seesaw Mechanism	10
3	Important Concepts and Variable Definitions	13
3.1	Jets	13
3.2	Cross Section and Luminosity	15
3.3	Pseudorapidity	15
3.4	p_T , $E_T^{\vec{miss}}$ and H_T	16
3.5	Displaced Vertices and Impact Parameter	17
4	CMS Detector	19
4.1	Tracking System	20
4.2	Calorimetry	22
4.2.1	Electromagnetic Calorimeter	22
4.2.2	Hadron Calorimeter	23
4.3	Muon Detector	23
4.4	Triggers	25
5	Model and backgrounds	27
5.1	Signal of Interest	27

5.2	Backgrounds	28
5.2.1	W+Jets Background	29
5.2.2	Drell Yan + Jets Background	30
5.2.3	$t\bar{t}$ Background	31
6	Methodology	33
6.1	MadGraph	33
6.2	Pythia	34
6.3	Delphes	35
6.4	ROOT	35
7	Event Selection Criteria	37
8	Analysis	41
9	Conclusions	49
Appendix A	Neutrinos and Seesaw Mechanism	51
A.0.1	Dirac Mass	51
A.0.2	Majorana Mass	52
A.0.3	Seesaw Mechanism	54

List of Figures

2.1	Particles of the Standard Model	6
3.1	Description of a jet at three different levels: partonic, hadronic and detector. Image taken from [13]	14
3.2	CMS detector coordinates. Image taken from [16]	16
3.3	Scheme of a displaced vertex. Image taken from [17]	18
3.4	Scheme of the impact parameter variable. Image taken from [18]	18
4.1	CMS detector. Image take from [19]	20
5.1	29
5.2	Feynman diagram for the W+jets Background	30
5.3	Feynman diagram for the DY+jets Background	31
5.4	Feynman diagram for $t\bar{t}$ Background	31
8.1	E_T^{miss} distribution for the signal and backgrounds	42
8.2	Distribution of diferent variables after cuts in the number of jets, taus and b-jets	45
8.3	Distribution of diferent variables after all the cuts	46
8.4	2D graphic: E_T^{miss} vs d_{xy}	47
8.5	2D graphic: $p_T(\tau)$ vs $ d_{xy} $	47

Chapter 1

Introduction

The Standard Model (SM) is a theory that collects our knowledge about the elementary particles and their interactions. Despite this theory is capable of explaining several physical phenomena that have been observed in experiments, there are some questions that this model do not answer. Thus, this theory is not complete. One example of the physical phenomena the SM does not explain are cosmological observations that suggest the existence of a new type of matter that is stable, massive and that does not interact with electromagnetic radiation, whereby it is called Dark Matter (DM). There is a disagreement between these astronomical observations and the theoretical predictions for the rotation velocity of stars and galaxies. For this reason, DM has been proposed. Unfortunately, the SM does not provide a particle that fulfills the required characteristics of DM. Other dilemma the SM has is related to the mass of neutrinos, the model predicts that it is zero. Nevertheless, the former is incorrect because the observations of neutrinos oscillations in multiple experiments demonstrate that neutrinos have mass [1, 2]. One additional fact that is very interesting and the SM can not explain is the observation of neutrinos with only left-handed helicity. .

Since the SM does not explain different phenomena, in particular the observation of only left-handed neutrinos, some models that extend the SM have been constructed. Some of these models propose the existence of heavy neutrinos with right helicity, which in some cases are postulated as candidates of DM [3, 4]. Additionally, these models propose a mechanism

by which neutrinos acquire mass. One of the most famous extension models of the SM, that propose the existence of heavy right-handed neutrinos, is the Seesaw Mechanism. If the existence of these particles is proved, not only the helicity symmetry of neutrinos would be restored, but also it would explain how they gain mass. The search of these particles has been performed in the experiments LEP [5], CMS [6] and ATLAS [7] without successful results.

Recently, it has been proposed a new mechanism of production of heavy neutrinos through the decay of the Higgs Boson [8] using the type I Seesaw mechanism. If the heavy neutrino mass is of the order of a few GeV the Higgs boson would travel a certain distance before decaying. As a consequence, the decay products are expected to have associated tracks with displaced vertices. For this reason, the presence of displaced vertices in the detector is an important signal to prove the model. Nevertheless, due to experimental restrictions of the available triggers in CMS and ATLAS, the theoretical analysis proposed in reference [?] is not achievable. Thus, in this project is proposed the search of the heavy neutrino when the Higgs boson is produced by a process denominated Vector Boson Fusion (VBF).

The observation of the Higgs decay into heavy neutrinos would be a firm prove of the Type I Seesaw mechanism [9], which would indicate the existence of physics beyond the SM associated to the mass of the neutrinos. The Type I Seesaw mechanism is the simplest extension of the SM that is capable of explaining the smallness of the neutrino with respect to other fundamental particles.

The main problem of detecting an event of interest is that the magnitude of its signal is significantly smaller with respect to processes from the SM. For this reason, the processes from the SM that have the same or similar final states as the signal are called backgrounds. For this reason it is fundamental to develop procedures in order to reduce the experimental backgrounds under the magnitude of the searched signal. These procedures usually use different variables that exploit the topology of the event and its kinematic characteristics. When a set of variables that potentially separate the signal from the background is determined, it is necessary to find the optimal values of them that allow to reduce as much as possible the background. Generally, the optimization studies use figures of significance, such as:

$$\frac{S}{\sqrt{S+B}}, \quad (1.1)$$

where S and B represents the expected event number of signal and background correspondingly.

This document is organized as follows. In 2 Chapter the State of the Art for this study is stated: the SM is described and the Seesaw mechanism is explained. Then, in the Chapter 3 the important concepts for this analysis, such as jet and cross section, are described. Additionally, the kinematical variables used in this analysis that have the potential of reducing the levels of backgrounds are defined and illustrated. Next, in the Chapter 4 there is information about the detector CMS, where is described how each of its parts functions and their specific tasks in the detector. The CMS detector is conformed by the tracking system, the electromagnetic and hadron calorimeters and the muon systems. There is also a brief description of the triggers performed at the CMS. In the Chapter 5 there is an exposition of the event of interest, it is described the topology of the signal and its possible final states. Then, the backgrounds for this signal are mentioned with their corresponding final states. In Chapter 6 there is a description of the software tools used in this analysis. The computational programs used are: MadGraph which makes a simulation of the event, Pythia which simulates the processes of hadronization of the signal, Delphes which simulates the behaviour of a multipurpose detector, and ROOT that is used to perform the analysis of the signal and backgrounds. In the next chapter, 7, the different preselection values imposed are enumerated. Then, all the required cuts on the variables are described with an explanation of why they are done with the corresponding values. In Chapter 8 there is information about the analysis that was performed, it shows the performance of different variables and their potential to reduce the backgrounds is discussed. Finally, at Chapter 9 the conclusions of this project are stated.

Chapter 2

State of the Art

2.1 Standard Model

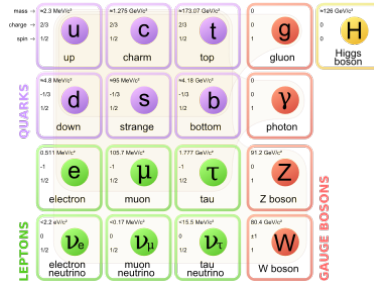
The SM is a theory that explains how the fundamental blocks of the universe interact through the fundamental forces of nature. This model is based on a quantum field theory which incorporates relativity and quantum mechanics. The SM also classifies the fundamental particles and the compound ones.

According to this model there are two types of fundamental particles in nature: bosons and fermions. Fermions are the particles that compound the matter, while bosons transmit the interactions through their exchange. Bosons have integer spin while fermions have half-integer spin. There are two classifications of fermions: quarks and leptons. The quarks particles have a characteristic property called color charge. There are three types of color charge referred as: blue, red and green. Quarks present a phenomenon called color confinement which causes that they can not be isolated singularly, so they can only be found in nature in group as hadrons. Thus, hadrons are defined as composite subatomic particles and there are two types of them: baryons and mesons. Baryons are conformed by three quarks and mesons by two quarks. The other type of fermions are leptons, which do not posses the color charge property.

The SM explains three fundamental interactions: electromagnetic, strong and weak, but it does not include the gravitational interaction. The electromagnetic interaction acts on particles that have electric charge, it is

transmitted by photons, and it has an infinite range. The strong interaction affects color charged particles (quarks) and it is mediated by gluons which carry color charge. The range of strong interaction is just around 10^{-15}m (the order of the diameter of a medium sized nucleus). The magnitude of strong interaction is big enough to maintain the nucleus of an atom together. The weak interaction appears in the radioactive decay, which is the process responsible for the decay of unstable nucleus. The radioactive decay is caused when there is a greater quantity of protons than of neutrons. The weak force is transmitted through three bosons W^\pm and Z^0 . Since the mass of each of these particles is relatively large, the weak interaction has a short range of around 10^{-18}m .

Figure 2.1: Particles of the Standard Model



The Figure 2.1 brings together the particles of the SM and specifies their properties. Fermions are grouped into three generations, each having two quarks and two leptons. Each member of a higher generation has a greater mass than the corresponding particle of the previous generation. The classification for quarks is the following: the first generation includes up and down quarks, the second generation strange and charm quarks, and the third generation bottom and top quarks. Each generation contains one quark with charge $-1/3$ (down-type) and other with charge $+2/3$ (up-type). For leptons, each generation includes one with -1 charge lepton and one neutral lepton (called neutrino) related to the correspond partner. Their classification is: first generation contains electron and electron neutrino, second muon and muon neutrino, and third tau and tau neutrino. The SM also postulates that for each known particle there exists another particle with the same value of mass and spin but opposite electric charge and

different color charge. This partner is called antiparticle.

Additionally, according to the SM, the fundamental particles acquire their mass through their interaction with a scalar field denominated Higgs field. The mediating particle of this field is the Higgs boson and it was discovered on 2012 as announced by the experiments CMS and ATLAS. As it was mentioned earlier, SM is not a complete theory since there are physical phenomena that this theory does not explain. For example, it predicts neutrinos have zero mass but the observations neutrino oscillations indicate the opposite. Moreover, the SM does not provide a possible candidate for DM and does not explain the asymmetry of the neutrinos helicity. For this reason, some theories that extend the reach of SM have been proposed. One simple extension of SM that can explain the smallness of neutrino masses is Type I Seesaw mechanism.

2.2 Neutrinos in the Standard Model

As it was mentioned earlier, the SM does not explain the reason why the mass of neutrinos is a factor of almost 10^{-6} smaller than the mass of the other fermions. Moreover the SM predicts that the mass of the neutrinos is zero. Additionally, it does not provide an explanation to the fact that only left-handed neutrinos have been observed in nature. In this section we are going to work on possible solutions to these problems.¹

2.2.1 Dirac Mass

First, we start by studying the Dirac mass term of a free fermion. The Lagrangian equation for a fermion particle is given by the expression:

$$L = \bar{\psi}(i\gamma^\mu\partial_\mu - m)\psi, \quad (2.1)$$

where ψ is the Dirac Spinor. From this Lagrangian expression it is possible to see that in the SM the mass is included through the second term in the equation which is called “Dirac mass term”:

$$m\bar{\psi}\psi \quad (2.2)$$

¹The detailed calculations of the theory explained here are stated in A

We can write the Dirac Spinor as a sum of its left- and right- chiral states:

$$m\bar{\psi}\psi = m(\bar{\psi}_L + \bar{\psi}_R)(\psi_L + \psi_R) = m\bar{\psi}_L\psi_R + m\bar{\psi}_R\psi_L \quad (2.3)$$

In the last expression we used the fact that: $\bar{\psi}_L\psi_L = \bar{\psi}_R\psi_R = 0$ which is proved in Appedix A. It can be seen from Equation 2.3 that a massive particle must have both quiral states: left and right. Thus, the Dirac mass can be interpreted as the coupling constant between the two chiral states. Since right-handed neutrinos had been never observed in nature, it is expected that neutrinos have zero mass. Although, experiments of neutrino oscillations indicate that neutrinos have a small mass of the order of MeV. The former implies either the existence of a right-handed neutrino which is responsible for the mass of the neutrino, or that there exists other sort of mass term [10].

2.2.2 Majorana Mass

The Majorana Mechanism is based on expressing the mass term in the Lagrangian in only the left-handed chiral state terms. To do this we start by decomposing the wavefunction into its left and right chiral states in the Dirac Lagrangian [11]

$$\begin{aligned} L &= \bar{\psi}(i\gamma^\mu\partial_\mu - m)\psi \\ &= (\bar{\psi}_L + \bar{\psi}_R)(i\gamma^\mu\partial_\mu - m)(\psi_L + \psi_R) \\ &= i\bar{\psi}_L\gamma^\mu\partial_\mu\psi_L - \bar{\psi}_L m\psi_R + i\bar{\psi}_R\gamma^\mu\partial_\mu\psi_R - \bar{\psi}_R m\psi_L \end{aligned} \quad (2.4)$$

Since $\bar{\psi}_L\psi_L = \bar{\psi}_R\psi_R = 0$ and $\bar{\psi}_R\gamma^\mu\partial_\mu\psi_L = \bar{\psi}_L\gamma^\mu\partial_\mu\psi_R = 0$ as it is explained in the Appendix A. Now, we can replace the expression of this Lagrangian in the Euler-Lagrange equation:

$$\frac{\partial L}{\partial(\partial\phi)} - \frac{\partial L}{\partial\phi} = 0 \quad (2.5)$$

By doing this we find that the two equations of motion for the fields are two coupled Dirac equations for the right- and left- handed fields:

$$i\gamma^\mu \partial_\mu \psi_L = m\psi_R \quad (2.6)$$

$$i\gamma^\mu \partial_\mu \psi_R = m\psi_L \quad (2.7)$$

In the formulation of the SM the mass of the neutrino is zero, in this case we obtain two equations which are called “Weyl equations”:

$$i\gamma^\mu \partial_\mu \psi_L = 0 \quad (2.8)$$

$$i\gamma^\mu \partial_\mu \psi_R = 0 \quad (2.9)$$

The former means that neutrinos can be described using two two-component spinors that are helicity eigenstates. These eigenstates represent two states with definite and opposite helicity which correspond to the left- and right-handed neutrinos. However, since we have not observed a right-handed neutrino we just represent the neutrino as a single left-handed massless field. [10]

Majorana worked out a way to describe a massive neutrino just in terms of it's left-handed field. This calculation is performed in the Appendix A. The objective of Majorana was to write the Equation 2.7 as 2.6 by finding an expression for ψ_R in terms of ψ_L . By doing some manipulations of the Equation 2.7 we find that it can be written as:

$$i\gamma^\mu \partial_\mu C\bar{\psi}_R^\top = mC\bar{\psi}_L^\top, \quad (2.10)$$

where C is the operator charge conjugation operator. Now, the Equation 2.10 would have the same structure as Equation 2.6 if the right-handed term is imposed to be:

$$\psi_R = C\bar{\psi}_L^\top \quad (2.11)$$

The former assumption requires $C\bar{\psi}_L^\top$ to be right-handed, this is proved in the Appendix A. Thus, the complete Majorana field can be written as:

$$\psi = \psi_L + \psi_R = \psi_L + C\bar{\psi}_L^\top \quad (2.12)$$

Defining the charge-conjugate field as: $\psi_L^C = C\bar{\psi}_L^\top$, we get for the expression of the complete Majorana field:

$$\psi = \psi_L + \psi_L^C \quad (2.13)$$

The implications of requiring the right-handed component of ψ to satisfy the Equation 2.13 can be studied by taking the charge conjugate of the complete Majorana field.

$$\psi^C = (\psi_L + \psi_L^C)^C = \psi_L^C + \psi_L = \psi \quad (2.14)$$

Having in mind that the charge conjugation operator turns a particle state into an antiparticle state, it can be deduced that a Majorana particle is its own antiparticle. Since the charge conjugation operator flips the sign of electric charge, a Majorana particle must be neutral. Thus, the neutrino is the only fermion that could be a Majorana particle.

Majorana Mass Term

In Equation 2.3 we saw that the mass term in the Lagrangian couples the left and right chiral states of the neutrino. Replacing the expression we found in Equation 2.11 for the right-handed component of the neutrino field in the mass term of the Lagrangian we get the equation 2.15 [11]. In this equation we denoted the Dirac Spinor of neutrino as ν . Having in mind that the hermitian conjugated of the first term in the equation is identical, we normalize the Lagrangian and obtain:

$$L_{Maj}^L = m\overline{\nu}_L\nu_L^C + m\nu_L^C\overline{\nu}_L = \frac{1}{2}m\nu_L^C\overline{\nu}_L \quad (2.15)$$

2.3 Seesaw Mechanism

As it was mentioned before, in the case that the right-handed chiral field does not exist there can be no Dirac mass term. However, we can have a Majorana mass term in the Lagrangian (associated to a left-handed quiral field) so the neutrino would be a Majorana particle:

$$L_{Maj}^L = \frac{1}{2}m_L\nu_L^C\overline{\nu}_L \quad (2.16)$$

In order to let the neutrino to have mass, a right-handed neutrino that interacts only with gravity and the Higgs field must exist. If we consider

that a right-handed chiral neutrino can exist, we would have to add different terms to the Lagrangian. First, if we assume that it is possible to write a left-handed Majorana field, we have for the first term:

$$L_L^M = m_L \overline{\nu_L} \nu_L^C + m_L \overline{\nu_L^C} \nu_L \quad (2.17)$$

Additionally, we have to include a similar term which is the right-handed Majorana field:

$$L_R^M = m_R \overline{\nu_R} \nu_R^C + m_R \overline{\nu_R^C} \nu_R \quad (2.18)$$

We also have to add Dirac mass terms in order to study the most general Lagrangian: the first Dirac mass term we mentioned on this section (Equation 2.19) and another one that comes from the charge-conjugate fields (Equation 2.20) [10]:

$$L = m_D \overline{\nu_L} \nu_R + m_D \overline{\nu_R} \nu_L \quad (2.19)$$

$$L = m_D \overline{\nu_R^C} \nu_L^C + m_D \overline{\nu_L^C} \nu_R^C \quad (2.20)$$

Since the hermitian conjugate of each equation is identical, we can write the most general mass term as a sum of the Lagrangians we just mentioned:

$$L = \frac{1}{2} \left(m_L \overline{\nu_L} \nu_L + m_R \overline{\nu_R} \nu_R + m_D \overline{\nu_R} \nu_L + m_D \overline{\nu_L} \nu_R \right) \quad (2.21)$$

The former equation can be written as a matrix equation:

$$L_{mass} \propto \begin{pmatrix} \overline{\nu_L^C} & \overline{\nu_R} \end{pmatrix} \begin{pmatrix} m_L & m_D \\ m_D & m_R \end{pmatrix} \begin{pmatrix} \nu_L \\ \nu_R^C \end{pmatrix} \quad (2.22)$$

Equation 2.22 expresses the Lagrangian in terms of the left and right chiral states. These states do not have a definite mass because the matrix is not diagonal. Thus, the left and right chiral states do not correspond to the physical particles (which have a definite mass). Instead the real particles are a superposition of the mass eigenstates. In order to find the mass eigenvalues we need to diagonalize the M matrix (the one in the middle of the former equation). This calculation is explained in Appendix A. We find the mass eigenstates are given by the expression:

$$m_{1,2} = \frac{1}{2} \left[(m_L + m_R) \pm \sqrt{(m_L - m_R)^2 + 4m_D^2} \right] \quad (2.23)$$

The fact that the SM does not allow a Majorana left-chiral mass term implies $m_L = 0$. Next, we are going to study the expression of the mass eigenstates m_1 and m_2 . When we choose $m_R \gg m_D$, we get for the mass eigenvalues:

$$m_1 = \frac{m_D^2}{m_R} \quad (2.24)$$

$$m_2 = m_R \left(1 + \frac{m_D^2}{m_R^2} \right) \approx m_R \quad (2.25)$$

From both equations above we can deduce that if there a neutrino with mass m_2 very large exists, then the other neutrino must have a small mass. The former fact is the reason why this mechanism is called “Seesaw”: the mass of each physical neutrino is controlled by the mass eigenvalues in a way such that when one neutrino is light the other is heavier [11]. Now, the neutrino mass eigenstates are given by the following expresions:

$$\nu_1 \propto (\nu_L + \nu_L^C) - \frac{m_D}{m_R^2} (\nu_R + \nu_R^C) \quad (2.26)$$

$$\nu_2 \propto (\nu_R + \nu_R^C) + \frac{m_D}{m_R^2} (\nu_L + \nu_L^C) \quad (2.27)$$

The Equations 2.26 and 2.27 show that ν_1 is mostly the left-handed light Majorana neutrino while ν_2 is the heavy sterile right-handed neutrino. This is the explanation that the Seesaw Mechanism gives to the fact that the neutrino is much lighter than the other fermions.

Chapter 3

Important Concepts and Variable Definitions

3.1 Jets

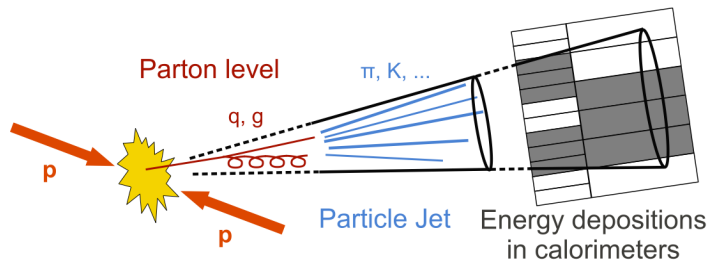
A jet can be defined as a high energy shower of stable particles that comes from fragmentation of quarks or gluons [12]. The initial quarks and gluons in the process are known as “initial partons”. Due to that initial partons are colour charged, they can not be isolated singularly (this phenomenon is called “colour confinement”). Since it is not possible for coloured particles to be isolated they must go through a non-perturbative process that converts them into colour neutral particles. This process is called “hadronization” and there are different models to explain it. According to the string model, the confining nature of strong interaction increases the potential colour in a proportional way as the distance between the initial partons. When the distance reaches a certain critical value, it is energetically favourable to produce a quark pair from the vacuum. Finally, by this process the initial colour charged particles are converted into bound colour-singlet hadronic states.

Despite jets may display a structure with properties that could indicate which were the initial partons interacting, they are hard to study individually when there is a numerous quantity of them in an event. The former

is because it is almost imposible to associate all particles in an event final state to a single initial parton. The reconstruction of jets depends of elements like the fragmentation process, detectors effects, among others. Thus, there exist algorithms which cluster some particles in a final state so that it is possible to determine properties as 4-momentum and jet shapes. The objective of these algorithms is to determine the inital interacting partons and approximate its directions and energies.

According to the reconstruction algorithms we can define a jet at three different levels. At parton level a jet can be understood as a quark or a gluon. At hadronic level can be referred to the hadrons produced due to the hadronization process, like kaons or pions. Finally, at a detector level a jet can be understood as a set of reconstructed tracks spatially associated with energy deposited in the calorimeters [14]. The reconstruction algorithms that are going to be used for this analysis consist in the use of mathematical cones that enclose the regions where a large quantity of particles are detected. The radius of the cone must be large enough to enclose all the particles coming from the initial quark or gluon, and must be small enough to not include other particles that belong to a different jet. The three level definitions just mentioned are illustrated in Figure 3.1. In this figure the mathematical cones used for the reconstruction of a jet is also showed.

Figure 3.1: Description of a jet at three different levels: partonic, hadronic and detector. Image taken from [13]



3.2 Cross Section and Luminosity

In High Energy Physics, the cross section σ represents the probability that a given physical process occurs. This quantity is proportional to the energy of the event production. The unit used for cross sections is the bar ($1b = 10^{-28}m^2$). The number of expected events of a certain interaction in a fixed target experiment is proportional to its cross section, the particle flux, and the number of atoms per cubic meter in the target multiplied by the length [15]. The inverse of the number of atoms per area is called “target constant F ” and it has the dimension of an area. Thus, it is possible to make an estimation of the number of interactions per second using:

$$\frac{N_{events}}{s} = \sigma \times \frac{N_{flux}/s}{F} = \sigma \times Luminosity \quad (3.1)$$

In the Equation 3.1 we defined the concept of luminosity, which is a measure of sensitivity and depends on the energy and on the beam dynamics. The luminosity is a quantity that is used to describe the performance of a particle accelerator. It has units of the inverse of cross section, which is known as inverse barns fb^{-1} and it is equivalent to ($1fb = 10^{-28}m^2$). In particle colliders the luminosity depends on different variables such as the number of particles per bunch N_b , the number of bunches in each beam κ_b , the revolution frequency f at the storage ring and the beam radii R of the bunches at the crossing point:

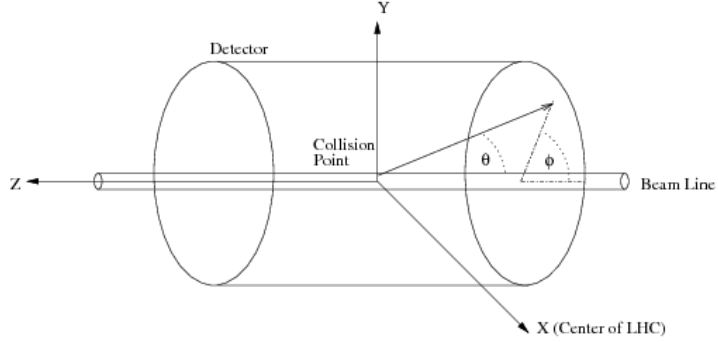
$$L = \frac{N_b^2 f \kappa_b}{4\pi R^2} \quad (3.2)$$

3.3 Pseudorapidity

The variable pseudorapidity is defined as a parametrization of the CMS and ATLAS detector coordinates. These coordinates are illustrated in the Figure 3.2:

The origin of the CMS and ATLAS coordinates coincides with the point in which a collision occurs in the detector. The polar angle is described by the parameter θ and it is measured with respect to the z axis. The azimuthal angle is denoted by Φ and it is measured in the xy plane from the x axis. The pseudorapidity is defined in terms of the polar angle as:

Figure 3.2: CMS detector coordinates. Image taken from [16]



$$\eta \equiv -\ln(\tan(\theta/2)) \quad (3.3)$$

The motivation to define and use this variable is that while $\Delta\theta$ is not a Lorentz invariant $\Delta\eta$ is. Moreover, the quantity of particles depending on the variable η is approximately uniform in a cylindrical detector.

3.4 p_T , $E_T^{\vec{miss}}$ and H_T

The quantity p_T is the transversal momentum and it is the projection of the linear momentum onto the xy plane. This variable is used instead of the linear momentum because the initial beams are moving just in the z axis (the initial momentum in the xy plane is zero), so when a collision is produced the interesting effects occur in the transverse plane.

As it was already mentioned, the momentum in the transverse plane is zero before the collision. Since the transverse momentum has to be conserved, after the collision it must also be zero. We can write the total momentum as the sum of the particles that are detected (visible particles) and the ones that are not detected (invisible particles), which can be expressed as:

$$0 = \sum_{i=1}^N P_T \vec{\tau}(i) = \sum_{j=1}^M P_T \vec{\tau}(j)^{visible} + \sum_{k=M}^{N-M} P_T \vec{\tau}(k)^{invisible} \quad (3.4)$$

The Equation 3.4 motivates the definition of a variable called “Missing transverse energy” (E_T^{miss}), which is defined as the sum of the transverse momentum of the invisible particles:

$$E_T^{miss} \equiv \sum_{k=M}^{N-M} P_T \vec{\tau}(k)^{invisible} = - \sum_{j=1}^M P_T \vec{\tau}(j)^{visible} \quad (3.5)$$

Finally, the variable H_T is defined as the sum of the transversal momentum of all the jets in the event, as it is showed in Equation

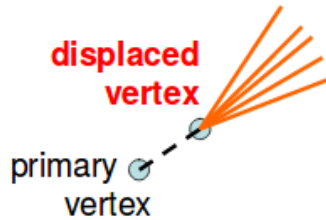
$$H_T = \sum_i^n P_T(jet_i) \quad (3.6)$$

3.5 Displaced Vertices and Impact Parameter

The vertex of a track is a variable of importance because it can be used to determine the position of the point of interaction and the momentum vector of the tracks emerging from the vertex. The vertex fit can also be used to check the association of tracks to a vertex, in other words, to determine if a track actually originates from a certain vertex. In order to determine the direction of the track connecting a primary and a secondary vertex we have to find the position of the secondary vertex. Some particles can pass through the detector without leaving tracks. However, when these undetected particles decay, the particles produced can be observed because they leave tracks on the detector. The point in which the product particles are detected is called a secondary vertex, and it is said that it is a displaced vertex. Figure 3.3 shows a sketch of a displaced vertex, where the path of the undetected particle is represented by a dotted line.

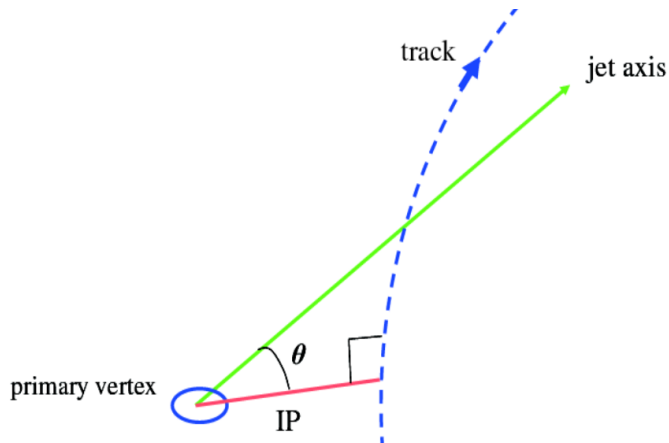
The impact parameter is defined as the closest distance between the vertex and the points of the track. A visualization of this is showed in Figure 3.4. In this image the track is represented by the blue dotted line, and the impact parameter by the red line. It can be seen that the impact

Figure 3.3: Scheme of a displaced vertex. Image taken from [17]



parameter line forms a right angle with the track. Using this characteristic it is possible to identify in a unique way the closest point of approach of the track to the vertex.

Figure 3.4: Scheme of the impact parameter variable. Image taken from [18]



Chapter 4

CMS Detector

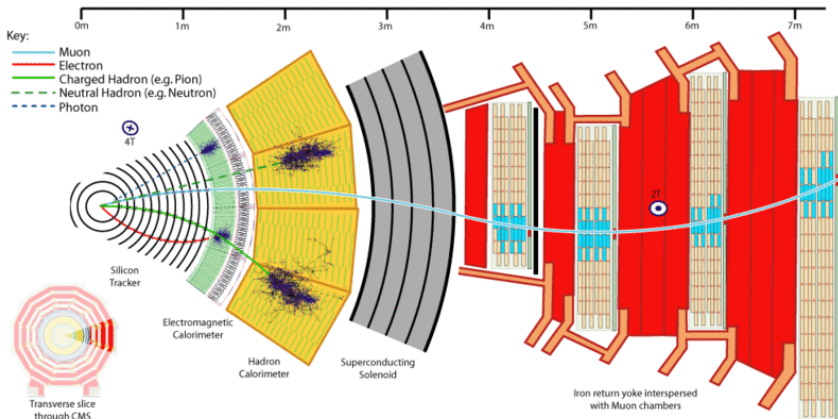
In this analysis we are going to perform simulations of collisions occurring at the CMS experiment, so we have to take into account the specific characteristics of this detector. For this reason the components of the CMS are going to be explained. The CMS is one of the seven experiments located at the Large Hadron Collider (LHC), which is the largest and most powerful particle accelerator in the world. This accelerator collides protons and heavy ions at very high energies of the order of 13 TeV and 6.37 TeV, respectively, with the objective of studying the elemental particles of the universe.

The LHC is conformed by a ring of almost 27 km of perimeter and by 7 detectors located at the different collision points of the ring. Two of these detectors are general-purpose detectors, and they are referred as experiments CMS and ATLAS (A Toroidal LHC ApparatuS). Both experiments share the same goals of searching physics beyond the SM. The physics program includes measurements of the Higgs boson, Supersymmetry searches, dark matter, detection of extra dimensions, among others. The difference between both experiments is that they use different designs and software. In the ATLAS detector the magnetic field is produced by a central toroid, two end toroids and a central solenoid, while the CMS detector is built around a superconducting solenoid magnet.

The CMS and ATLAS detectors have a cylindrical form in order to have the most uniform magnetic field possible. They are centered in the direction of the interacting beams and the collision point and have two

“end-caps” to cover the forward regions. These detectors are conformed by the same general components, from the inner part of the detector to the outer part. These components are: a tracking system, an electromagnetic and a hadronic calorimeter, and muon detectors. They also have magnets to curve the path of the electric charged particles, so it can be determined whether a particle has a positive or negative charge. Additionally, the measurement of the curve can be used to calculate the momentum of the charged particle. In Figure 4.1, there is a diagram showing the structure of the CMS detector. This image also shows the interaction of different particles with the parts of the detector.

Figure 4.1: CMS detector. Image take from [19]



4.1 Tracking System

Since every 25 ns there is a collision at the center of the CMS detector and almost 1000 particles are going to be produced, it is necessary to have a tracking system able to record measurements of all the particles that are produced. This tracking system must be located the nearest possible to the region where the collision occurs. This tracking system is used to measure the momentum and vertices of the particles with a high precision. The inner detectors are built with silicon detectors, with high granularity pixel

systems at the smallest radii, and silicon-strip detectors at larger ones [20].

The properties of the tracking system are: fast recording of measurements, toleration to high radiation doses, ensembled with light material and toleration of the severe conditions imposed by the low temperature at LHC (of almost 2 K). One of the major challenges for the inner detector parts is the control of aging effects because the damage produced by irradiation is severe. The silicon detectors are p-n junction diodes, so when a particle crosses the detector, it causes the liberation of electron-hole pairs, which move to the electrodes of the system. The tracking system in the CMS detector covers the range within $|\eta| < 2.5$, the region where most of the relevant particles for the analysis arrive.

The flux of particles arriving to a point in the detector depends of the distance from the center of collision to where the detector is located: as the flux crosses the detector material the quantity of particles decreases. Thus, the resolution of the tracking system does not need to be so high in the intermediate and end caps regions. For this reason, in the first region of the tracking system (the closest to the interaction point), there are silicon pixel detectors with cell size of $100 \times 150 \mu\text{m}^2$. The innermost layer of pixels is located as near to the beam as it is practical, this is at a radius around 4.5 cm.

The silicon pixels are expensive and have high power density. Additionally, the flux of particles at an intermediate region of the inner detectors is low enough to use silicon microstrips. Thus, in the region of radius greater than 20-55 cm the silicon pixels are replaced by silicon microstrips. These silicon microstrip are arranged in a special way to improve the resolution in the z axis. These barrel cylinders and end-caps disks, as the silicon pixels, cover the region of $|\eta| < 2.5$. The strip dimensions are or around $11\text{cm} \times 100\mu\text{m}$.

In the outermost region of the tracking system (at a radius greater than 55 cm) the particle flux is low enough to use larger-pitch silicon microstrips. The maximum size of these cells is $25\text{cm} \times 80\mu\text{m}$. There are 6 layers of these silicon microstrips modules in the barrel and 9 end-caps disks that also cover the region given by $|\eta| < 2.5$.

4.2 Calorimetry

Surrounding the tracking system of the CMS detector are located the electromagnetic and hadronic calorimeters. The calorimeters measure the energy of the incoming particles, by absorbing the particles and transforming them into heat. The priorities of the electromagnetic calorimeter is to measure precisely the energy of electrons and photons, to make measurements of their position and direction of movement. The priorities of the hadronic calorimeter are to make precise measurements of the jets energy and to cover a larger area of $|\eta| < 5$. The area covered has to be large with the purpose of attributing all the \vec{E}_T^{miss} to the particles that cannot be detected [20].

The electromagnetic and hadron calorimeters are made out of scintillation crystals. When a high energy particle goes through the detector, it collides with the nuclei of the material and generates a shower of particles. The product particles of this interaction excite the atoms in the material by making the electrons in the material go to a higher orbit. When each electron returns to the initial orbit, it emits a photon.

Then, the light emitted by the scintillator is measured by photodiodes, which have the function of converting the optical signals into electronic signals. The photodiodes mechanism is based on the photoelectric effect: the photons emitted by the scintillator arrive to the light-sensitive area of the photodiode and expulse electrons in this surface. Then these electrons are accelerated and strike a silicon diode target, which causes that more electrons get expelled of this surface. At the end, one obtains an amplification of the initial signal which is measured.

4.2.1 Electromagnetic Calorimeter

The electromagnetic calorimeter is an entirely active homogeneous calorimeter made of lead tungstate (PbWO_4) crystal. It has 61,200 crystal in the central barrel part and 7,324 in each of the two end-caps. As a consequence from the use of high density crystals, the calorimeter is fast, has fine granularity and is radiation resistant.

The lead tungstate crystal material was chosen for different reasons. First, it emits a short radiation length which is easy to record. Second,

it has small Moliere radius, which is defined as the radius of the cylinder surrounding the 90% of the shower's energy deposition. That leads to a compact calorimeter in size. Third, the lead tungstate crystal has short decay time constant, which allows the calorimeter to have a fast response. Lastly, it is resistant to high dosis of radiation. Moreover, due to the electromagnetic calorimeter is located within the solenoid, avalanche photodiodes are used as photodetector because they can operate under the magnetic field of 4T [20].

4.2.2 Hadron Calorimeter

Surrounding the electromagnetic calorimeter is located the hadron calorimeter. Its objective is to measure the energy and direction of jets. It is designed to detect the most possible particles product of a collision, so it is said that the detector has a hermetic coverage. The priority of this calorimeter is to determine as correct as possible the missing transverse energy ($E_T^{\vec{miss}}$). The hadron calorimeter is made out of plastic scintillator tiles with wavelength-shifting fiber. The wavelength-shifting is used to shift the wavelength of the light emitted by the scintillator in a the range in which the efficiency of the photodiodes is high [20].

The hadron calorimeter is restricted to fill the area between the outer cap of the electronic calorimeter and the magnet coil, this is $1.77\text{m} < R < 2.95\text{m}$. The layers of the scintillator tiles are alternately placed with layers of copper in the barrel to form the hadron calorimeter. The end-caps of the calorimeter covers the area of pseudorapidity given by $|\eta| = 3$ and $|\eta| = 5$.

4.3 Muon Detector

The muon system detector consists of several multi-layer large area gas-based detectors. The main objective of this detector is to take precise measurements of muon tracks. Since the muon system detector is located at the outermost part of the CMS the radiation level is receives is very low in comparison to the tracking system and the calorimeters. The CMS muon detector has three tasks: identify the muon particles, measure its momentum and triggering on them (this concept is explained in the next

subchapter). The layers of the muon detector alternate with layers of the yoke where the magnetic field returns, which is called flux-return yoke [20].

The flux-return yoke curves the path of the particles in the opposite direction as it was inside the copper layers. It also can be used for good resolution muon identification because it absorbs some hadrons with low energy. The high magnetic field applied and the flux-return yoke allows to take precise measurements of the muon momentum. The muon system detector surrounds the hadron calorimeter and, consists also of a barrel section and two end-caps.

The CMS detector has three types of gaseous particle detectors for muon measurements. In the barrel region where the neutron-induced background is low and the magnetic field is almost uniform, there are located drift chambers. The drift chambers are tubes each of 4 cm wide that contain a stretched wire immersed in a gas. When a muon crosses the chamber it hits the electrons of the atoms in the gas. Then, the free electrons arrive to the positive charged wire and it is measured an electronic signal. By measuring the time it takes for an electron to arrive to the cathode (known as drift-time) and the velocity of the free electrons (drift velocity) it is possible to determine the position of the initial muon [21, 12]. The drift chambers cover the region of pseudorapidity given by $\eta < 1.2$.

In the two-end caps regions there are cathode strip chambers (CSC). In these regions the muon rates and backgrounds levels are high and the magnetic field is large and non-uniform. The CSC uses the same principle as the drift chamber to measure the position of muons. The difference is that the CSC consist of anode wires crossed with cathode strips, these arrays are also immersed in a gas. When a charge particle crosses the detector, it hits the atoms of the gas expelling electrons. The free electrons are guided by the electric field and arrive to the anode wires, while the positive ions move towards the cathode [22]. The CSC have fast response time, fine segmentation and are radiation resistant. Thus they are able to take precise measurements of time and position. These detectors cover the area given by $|\eta| < 2.4$. Due to the fact that the tracking system and muon detectors take independent measurements of the muon momentum, it is possible to find errors and check both measurements [20].

An additional redundancy in the muon measurements is contributed by resistive plate chambers (RPC) in the barrel and the two end-caps regions.

It is similar to the other two muons detectors: it is conformed by two plates, one is the cathode and the other the anode and these plates are separated by a gas. When a charged particle crosses the detector, the resulting free electrons move to the anode. The electric signal is received by metallic strips after a precise time delay [23]. The set of hit strips gives a precise measurement of the muon position and momentum.

4.4 Triggers

Since at the LHC there are bunch crossings every 25 ns with a peak crossing rate of 31.6 MHz, nearly a billion proton-proton events are produced every second. Thus, it is necessary to decide to store or not store an event in order to reduce the computational resources use. Triggers have the task of applying a primary selection on the data at real-time. The triggers take the data and quickly decide which events that are interesting pass to the next phase of filtering. The triggers need to have a rejection factor of almost 10^7 . As a consequence, it allows to store just around 100-200 carefully selected events per second to be processed later.

The first triggering level uses a partial amount of the total information given by the detector and takes decisions in less than 3.2 ns. It reduces the data rate to nearly 100 kHz [24]. High level triggers use a network of thousands of processors and fast switches. They get the information gradually and use algorithms in order to reduce the amount of data. The final product is that at a rate of 150-200 Hz each event occupies around 1.5 Mb. The former leads to the LHC to have an annual data volume of around 10 PB [20]. After an event passes the first triggering level, the resulting data is transferred from the detector electronics into readout buffers. Then, the signal is processed and compressed while the events are studied by processors with several thousands of central processing units. The event then is directed to a single processor with the objective of performing detailed calculations of the critical parameters of the event and reduce the amount of data.

Chapter 5

Model and backgrounds

5.1 Signal of Interest

The model that was studied is based on a recently proposed new mechanism of production of heavy neutrinos through the Higgs Boson decay [8]. One favourable characteristic of this model is that in a natural scenario the mass of the heavy neutrinos can lie at the electroweak scale. The theoretical study of [8] propose the experimental search of the heavy neutrinos using a technique known as displaced vertices.

According to this model, when the mass of the heavy neutrinos is inferior than the mass of the Higgs, the latter can present novel decay channels. The Higgs boson can decay into a light and a heavy neutrino, followed by a subsequent decay of the heavy neutrino via a charged or neutral current interaction. Then, the decays of the heavy neutrino can be represented by: $N \rightarrow l^+ l^- \nu$ or $N \rightarrow l q q'$. Thus, there are two possible final states of the event of interest: two leptons, two jets (from the VBF process) and E_T^{miss} (due to the neutrino) or four jets (two of the VBF process and two from the quarks of the heavy neutrino decays), E_T^{miss} and one lepton. The first type of final state is going to be called leptonic signal, while the second will be named hadronic signal.

If the heavy neutrino has a mass of the order of a few GeV, the Higgs and heavy neutrino would travel a certain distance before decaying. Since both particles are not detected, the decay products are expected to have

associated tracks with displaced vertices. For this reason, the presence of displaced vertices in the detector is an important signal to prove this model because it could indicate the presence of the heavy neutrino in the detector. Nevertheless, in this model the resulting leptons have a low momentum. Thus, due to experimental restrictions of the available triggers in CMS and ATLAS, the theoretical analysis proposed in reference [?] is not achievable.

The High Energy Physics Group at Universidad de los Andes has proposed a technique that allows to study at the LHC the production of heavy neutrinos through the decay of the Higgs boson. While in the model proposed in [?] considers the production of the Higgs boson through the fusion of two gluons, we consider the Higgs production through the fusion of two vector bosons. These vector bosons (W^\pm, Z^0, γ) come from an interaction process between two quarks. Both quarks belong to protons from opposite beams that will collide in a particle accelerator. The former described process is known as Vector Boson Fusion (VBF) [25].

Finally, as a result of the fusion of the two vector bosons, a Higgs boson is produced and the initial quarks that interacted manifest themselves as jets with high transverse momentum in opposite hemispheres of the detector. For this reason, in Experimental Particle Collider Physics the events in which two jets of high transverse momentum are detected in opposite hemispheres of the detector and with a high separation of pseudorapidity are labeled as candidates of processes of VBF. The Feynman diagrams illustrating the processes already described is shown in Figure 5.1, where 5.1a is the hadronic signal and 5.1b illustrates the leptonic signal. Since it is expected that the hadronic signal have a larger cross-section than the leptonic signal, in this analysis we simulated only the hadronic signal.

5.2 Backgrounds

The main problem of detecting an event of interest is that the magnitude of its signal is significantly smaller with respect to some other processes from the SM. For this reason, the processes from the SM that have the same or similar final states as the signal are called backgrounds. Thus, it is fundamental to develop procedures in order to reduce the experimental background under the magnitude of the searched signal. These procedures

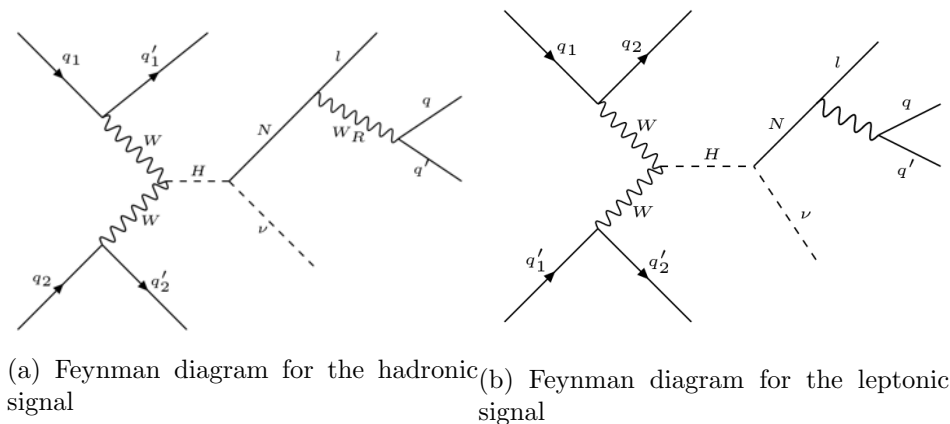


Figure 5.1

usually use different variables (like the ones explain in the chapter 3) that exploit the topology of the event and its kinematic characteristics. When a set of variables that separate the signal from the background is found, it is necessary to find the optimal values of them that allow to reduce as much as possible the background.

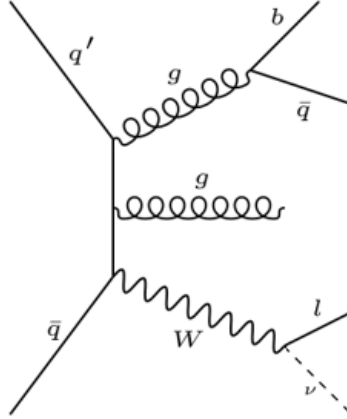
The signal of interest that was described had two possible final states. For the hadronic signal: two leptons, two jets and $E_T^{\vec{miss}}$ and for the leptonic signal: four jets, $E_T^{\vec{miss}}$, and one lepton. Thus, the main backgrounds of the signal that have a similar final state are the W+jets background and the DY+jets background. In a inferior magnitude there is other background that comes from the top pair production, referred as $t\bar{t}$.

5.2.1 W+Jets Background

The events in which is produced a W boson with jets has a large probability to occur in the collisions at the LHC. The W decay determines the final state of this event. The 64 % of the times the W boson has a hadronic decay and while the rest 36% times has a leptonic decay [14]. In leptonic decays, the W boson desintegrates into a lepton and a neutrino. Sometimes, in these events the particles comming from the interaction of the initial hadrons can produce a spontaneous radiative emission, which then

is detected as a jet. It is said that this kind of jet comes from an Initial State Radiation (ISR). Thus, when the boson W decays leptonically, the final state is conformed by a lepton, $E_T^{\vec{miss}}$ (comming from the neutrino) and jets from ISR. The Feynman diagram is shown in Figure 5.2.

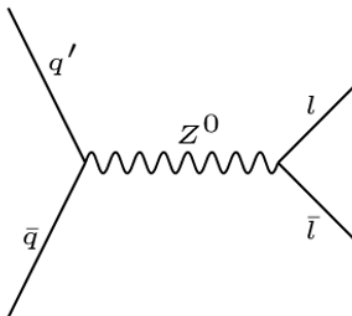
Figure 5.2: Feynman diagram for the W +jets Background



5.2.2 Drell Yan + Jets Background

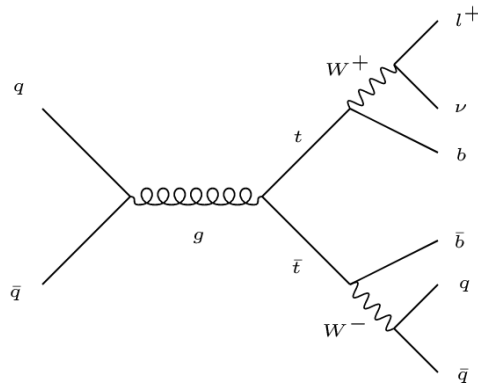
Other background for our signal of interest comes from the Drell Yan process. In this process a quark and an antiquark coming from the initial interacting hadrons annihilate each other and this produce a virtual photon or a Z boson. The concept virtual photon means that this particle is created for a very short period of time. We studied this process only when the Z boson decays into a pair lepton-antilepton, because in this case the final state is the most similar to the one of the signal. Specifically, we considered the events were the Z decays into a pair tau and antitau ($\tau\bar{\tau}$). This process was simulated with the presence of a jet from ISR. Thus, the final state is conformed by one tau, jets (from the ISR process), $E_T^{\vec{miss}}$ (from the erroneous identification of the one of the taus). The Figure 5.3 shows the Feynman diagram for this process.

Figure 5.3: Feynman diagram for the DY+jets Background



5.2.3 $t\bar{t}$ Background

Other background for our signal of interest is produced by the the top anti-top creation pair. These events are produced when a gluon coming from the interaction of two colliding protons that decays into a pair top-antitop particles. A Feynman diagram for this background is showed in Figure 5.4. This figure shows that the final state of this event has three leptons, MET (coming from the neutrino) and one characteristic jet associated to the hadronization of a b quark. Since the signal does not have the presence of a quark b, this background can be strongly reduced by making the filter of number of bjets equal to zero.

Figure 5.4: Feynman diagram for $t\bar{t}$ Background

Chapter 6

Methodology

The objective of this project was to make a phenomenological study that allow the identification of a signal with the presence of a heavy neutrino in the experiments of the LHC. For this reason, the proposed methodology consisted in the use of different computational programs to simulate the signal and its background as it should be produced and measured at the CMS detector. Next, this data must go through a statistical analysis. The programs that were used to simulate the signal were MadGraph and Pythia. Then, the program Delphes is used to simulate the behavior of the multi-purpose CMS detector. Lastly, the statistical study of the data was developed with the software ROOT, which determined the potential variables that could differentiate the signal and background. In the next paragraphs each program is going to be described, including the fundamental physical basis on which the program is constructed and its specific task in the development of the project.

6.1 MadGraph

The first program that was used is MadGraph, which is a generator of events that simulates the collisions of particle beams, which in our case are protons. MadGraph is written in Python programming language. The physical processes that MadGraph can simulate include processes from the SM and from physics beyond the SM that are based on certain theoret-

ical models such as Supersymmetry. This program incorporates diverse physical parameters in order to include all the necessary elements to make phenomenological studies: it calculates the cross section of a certain event, it generates events with strong interactions (including possible decay of particles) and it offers relevant tools to manipulate the events and to make their posterior analysis [26].

Madgraph uses perturbation theory to perform production calculations and to generate physical processes. The parameter entries are controlled in configuration files that are called input cards. These cards are use to modify essential variables in the production of the events, for example: the type of particles that will collide, the energy of the collision, number of events that are going to be simulated, mass of the generated particles, final states, among others. At the level of event generation it is possible to make basic cuts of minimal and maximal values of some kinematic variables. Moreover, the lastest version of MadGraph (MadGraph 5) has an useful characteristic: it can give an output file with matrix elements that can be used directly in the program Pythia.

In order to produce an event of physics beyond the SM one has to describe the physical model in the form of a Lagrangian , a list of fields and parameters. Then use the former elements as parameters input of the MATHEMATICA-based package FEYNRULES. Finally, FEYNRULES returns the Feynman rules corresponding to the Lagrangian of the model, which are used as input of MadGraph [27].

6.2 Pythia

The second computational program that was used is called Pythia. This program receives as parameter input the file generated by the software MadGraph. Pythia incorporates a set of physical models to develop the evolution of a few-body system into a complex multi-particle final state. Thus, the task of the Pythia in the project was to simulate the processes of hadronization of quarks and gluons [28].

6.3 Delphes

The next program that was used receives as input the events produced by Pythia and it is called Delphes. This software makes a realistic simulation of the multipurpose CMS detector performance as it would happen if there was occurring such an event at CMS. The simulation includes a system of track reconstruction immersed in a magnetic field, an electromagnetic calorimeter, a hadronic calorimeter and a muon detection system.

Delphes takes into account the systematic errors that can be generated by the detector, which can be caused by multiple factors such as the resolution of the detectors. This program contemplates different characteristics of the event in the experiment: detector geometry, the track of the charged particles in the magnetic field, reconstruction of the events, and efficiencies of the reconstruction and particle identification. Due to that the proposed analysis includes the systematic errors that can be generated by the detector, it can be implemented in the experimental studies at the LHC [29].

6.4 ROOT

The analysis of the simulated data was developed using the software ROOT. This software was created by the CERN laboratory. ROOT is written in the programming language C++ and it was designed to analyze data in particle physics. This program provides all the necessary tools to efficiently process large data, make statistical analyses, and visualize and store data. The program includes a numerous quantity of mathematical and statistic functions, numeric algorithms and methods for analysis of data regression. One key tool ROOT has are the histograms that can even use multidimensional data and estimate their density. The histograms can be manipulated, offer statistical information and can make data regression [30].

The program ROOT receives as input parameter complementary information that allows it to do the best analysis of the signal: characteristics of the detector or configuration settings that were made in the simulations. ROOT includes other components like a command interpreter that makes quicker the analysis process and a graphic interface which contains a flexible set of tools. The former means that the set of tools can be modified

using GUI Builder (the graphic interface constructor). This software can be used to analyse real or simulated data that have the same structure and consist of many events.

Chapter 7

Event Selection Criteria

The analysis of the simulated data started by imposing a minimum value of 20.0 GeV on p_T for b-jets and taus, and of 30.0 GeV on jets that are not associated to taus or b quarks. The low values required on p_T are imposed in order to preselect the interesting particles. After this was done, we required a minimal distance of separation between taus and muons, taus and electrons, and taus and jets. The former was because we have to be sure that taus do not overlap with other objects, so the performed analysis can evade to commit errors such as tagging incorrectly a particle. To do this, one has to impose a minimal value on the variable called minimal separation distance ΔR , which is given by the Equation 7.1. The minimal value imposed on this variable was 0.3 for taus with muons, electrons and jets.

$$\Delta R \equiv \sqrt{\Delta\eta^2 + \Delta\phi^2} \quad (7.1)$$

Since we considered that the event of interest is generated by a process of VBF, in the analysis was necessary to find the two possible jets that are related to the two VBF jets. This was done by searching two jets that satisfy the conditions of having a minimal value on p_T of 50.0 GeV and η greater than 5.0 each. The condition of minimal values on p_T and η is required because it is expected that the VBF jets have a large momentum and that they are located at the end-caps of the detector. Then, an algorithm was performed to select the pair of jets that have the largest sum of

the mass of all possible combinations of jets pairs in each event. Finally, a minimal value of 100 GeV is required for the sum of the jets. That is how the two jets from the VBF process are determined. From both jets, the one with the highest momentum is referred as the leading jet, and the other is known as the subleading jet. The required values to identify the VBF jets are part of the preselection process.

After the former preselection process is made, we have to find the minimal or maximum values of variables that allow to reduce the background of the signal at maximum. These minimal and maximum required values are known as cuts. The first cut imposed in the analysis was on the number of jets. It was required a maximum number of 5 jets because the signal is expected to have 4 jets. An additional jet is included in order to find the best two VBF jets. The second cut imposed was the presence of just one tau, due to the fact that this is a characteristic expected for the hadronic signal.

Next, the third cut is imposed by requiring the number of b-jets to be zero. The former is done to reduce drastically the $t\bar{t}$ background because it has in the final state b-jets. The following cut made was on the variable $E_T^{\vec{miss}}$: it was required a value greater than 20 MeV. The former is because in the hadronic signal the neutrino is the only source of $E_T^{\vec{miss}}$, thus it is expected that this variable has a low value for our signal. Then, it was performed a cut on the absolute value of η of the tau of maximum 2.1. This value was chosen because the tracking detector covers the range of $|\eta| < 2.5$. Since the reconstruction cones of the taus have a radius of around 0.4, one has to impose a maximum value on $|\eta|$ of maximum $2.5 - 0.4 = 2.1$ so the reconstruction algorithms are correctly applied in the area covered by the track detector.

After it was imposed a cut on the $E_T^{\vec{miss}}$ variable, the cuts motivated by the VBF process were performed. The first cut guarantees that there are minimum two jets that satisfy the condition on p_T to be candidates of VBF jets. Next, it is required that the product of eta of both jets is negative. This implies that both jets are located at the opposite hemispheres, as it is expected for both of the VBF jets. Next, it is imposed a minimal value of the difference in η for both jets, referred as $\Delta\eta$. The minimal value on $\Delta\eta$ was required to be 3.8, since the VBF jets should have a large difference in the pseudorapidity value. Finally, a cut in the sum of the mass of the VBF

jets, known as dijet mass, was made. It was imposed a value of minimum 500.0 MeV on the dijet mass, due to the fact that the VBF jets have a large momentum, and this is proportional to the mass.

The table 7.1 shows the preselection values imposed that were mentioned on the initial paragraphs of this chapter. Additionally, the table 7.2 shows all the cuts that were performed on the data in order to reduce as much as possible the backgrounds.

Table 7.1: Preselection criteria

Variables	Value
$p_T(b-jets) \ \& \ p_T(\tau)$	$>20.0 \text{ GeV}$
$p_T(jets)$	$>30.0 \text{ GeV}$
$\Delta R(\tau, e), \Delta R(\tau, \mu) \ \& \ \Delta R(\tau, jets)$	>0.3
$P_T(VBF_jet)$	$>50.0 \text{ GeV}$
$\eta(VBF_jet)$	>5.0
diJetMass	$>100.0 \text{ GeV}$

Table 7.2: Cuts on different variables

Variables	Values
n(jets)	<5.0
n(τ)	$= 1$
n(b-jets)	$= 0$
$ \eta(\tau) $	<2.1
\vec{E}_T^{miss}	$>20.0 \text{ GeV}$
n($p_T(jet) > 50.0$)	≥ 2
$\eta(jet_l)\eta(jet_s)$	<0
$\Delta\eta$	>3.8
diJetMass	$>500 \text{ GeV}$

Chapter 8

Analysis

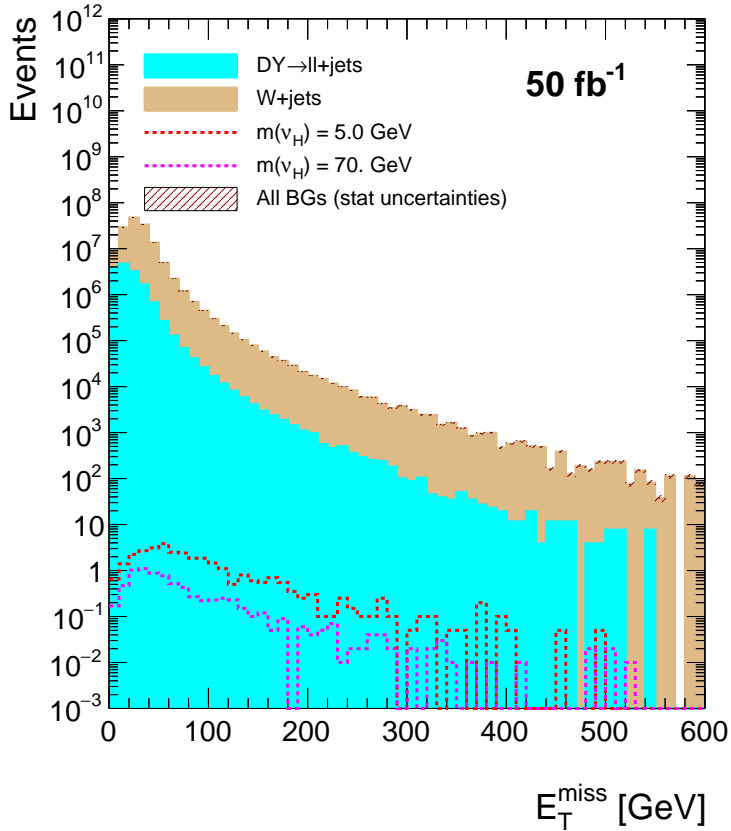
Since MadGraph needs as input parameter the mass of the heavy neutrino, two signals were simulated. One signal was made with a value of 5.0 GeV for the heavy neutrino mass, while the other assumed this mass to have a value of 70.0 GeV.

In order to study the performance of a variable to reduce the backgrounds, histograms of this variable were made for each signal and background. These histograms are then placed on the same graphic and each one is normalized to the corresponding luminosity. This normalization makes possible to compare the performance of the variable among them. The luminosity of the accelerator is given by 50 fb^{-1} . If each histogram is not normalized it will depend on the size of the simulated sample. In these graphics the bins of one background are located above the corresponding bins of the other background. Thus, the total background is given by the curve of the background at the top. The background uncertainty is represented by a dashed line at the top of the background histograms. These kind of graphics are called stacked plots. The graphs shown here include just the W+jets and DY+jets backgrounds because these are very large compared to the $t\bar{t}$ background, and reducing them is already a difficult task.

The analysis started by studying the distribution of different variables after the preselection cuts and some cuts on three variables: number of jets, taus and b-jets. The first variable studied was $E_T^{\vec{miss}}$, and its stack plot is shown in Figure 8.1. The graphic shows that the amount of background is

much larger than both signals. Moreover, the distribution of the variable is similar for the signals and backgrounds. This implies that a cut on this variable would reduce the background in a similar way as it would reduce the signal. Thus, it is not possible to find an optimal cut value of MET.

Figure 8.1: E_T^{miss} distribution for the signal and backgrounds



Next, we studied the distribution of more variables in order to be able to find the optimal cut values. The variables are H_T , diJetMass and the p_T of the tau, and they are shown in the Figures 8.2a, 8.2b and 8.2c. It is possible to see that the distribution of these variables is similar for the signals and backgrounds. As a consequence, a set of optimal values of cuts

on these variables that allows to reduce the background below the signal can not be determined.

Then, all the cuts mentioned in the Chapter 7 are imposed. These cuts include the ones related to the VBF process and the results are showed in the following graphics. The variables H_T , diJetMass and $p_T(\tau)$ are shown in the figures 8.3a, 8.3b and 8.3c. In these graphics, one can see that after imposing all the cuts the amount of signal and backgrounds reduces drastically.

One fact that can explain the reason why the VBF cuts do not allow to reduce significantly the background compared to the signal is the similar values of mass of the Higgs boson and the Z boson. The production mechanism of a Higgs boson is identical to the Z gamma production mechanism because the mass difference between the Higgs boson and the Z boson is just 30 GeV. Thus, the characteristics of the VBF jets in the events are similar and it is difficult to distinguish both VBF topologies. In the case that the heavy neutrinos are produced by the decay of a particle heavier than the Higgs boson, this heavier particle must be the result of the interaction of more energetic VBF jets. Thus, in this case it is expected that the detected VBF jets would be more energetic, which would lead to differentiate both final states.

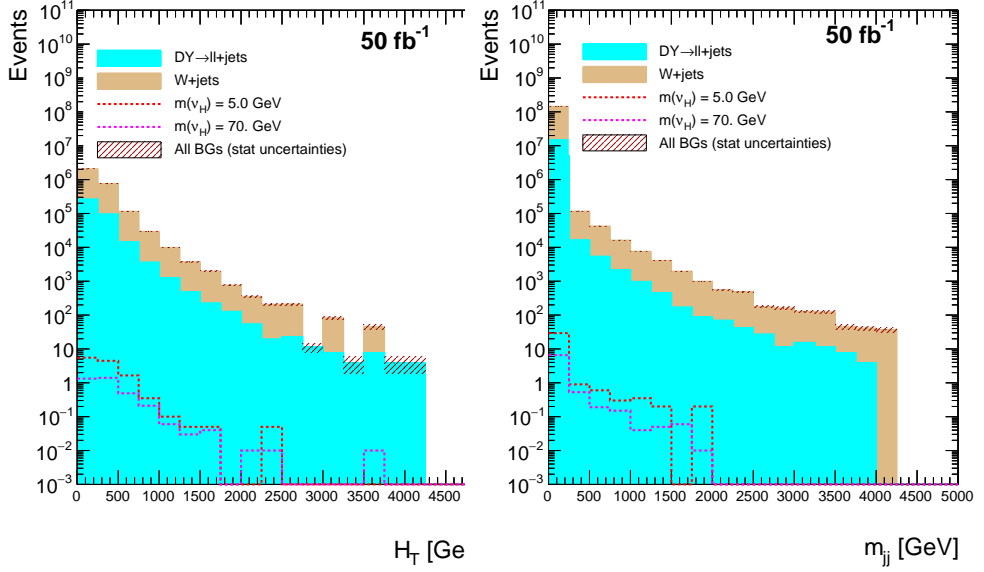
Since it was expected that the resulting tau in the signal had an associated track with a displaced vertex, some 2D plots were made using this variable. The value of the impact parameter for the tau was found by making a minimization process on the distance between the tau and the tracks, so the track associated to each tau is determined.

First, we studied a graphic on which the x axis represents $E_T^{\vec{miss}}$ and the y axis the impact parameter (d_{xy}) is shown in the Figure 8.4. The two graphics at the left of this figure correspond to the signal events, one assuming a mass of the heavy neutrino of 5.0 GeV, and the other of 70.0 GeV. The range of the y axis for both graphics is just from -1.0 to 1.0. The left graphics at the right of the figure correspond to the W+jets background and DY+jets background. These graphics have a range in the y axis from -8.0 to 8.0. It can be seen that for our signals the value of the impact parameter is almost zero. This implies that it is not possible to make a cut on this variable to reduce the background as it was expected.

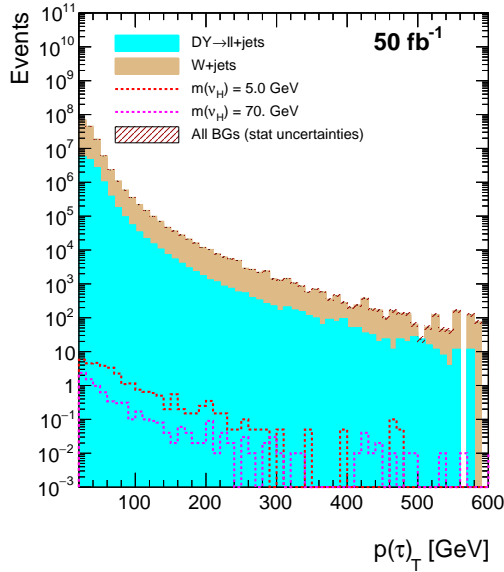
The other 2D graphic studied is shown in the Figure 8.5, where the x

axis represents the absolute value of the impact parameter and the y axis the transversal momentum of the tau. As in the previous figure 8.4, the y-axis for the analysis has a range between -0.1 to 0.4. Unfortunately, it is not possible to obtain relevant information from this figure.

Thus, in the end we obtain that our signals of interest have a low value on the impact parameter variable while it was expected the opposite. Now, possible facts that can explain the difference between our results and what was expected are discussed. In the first place the samples of signal are small compared to the sample size of background. Both simulated signals consist of 10000 events while the W+jets and DY+jets background samples consist of millions of events. Thus, we have a small statistical sample and it may be necessary to generate more signal events to make a study. On the other hand, it seems that Delphes does not reconstruct correctly the secondary vertices, which could explain the results of such a low impact parameter for the signal. If this problem is solved, a cut on the impact parameter value would strongly reduce the amount of background.

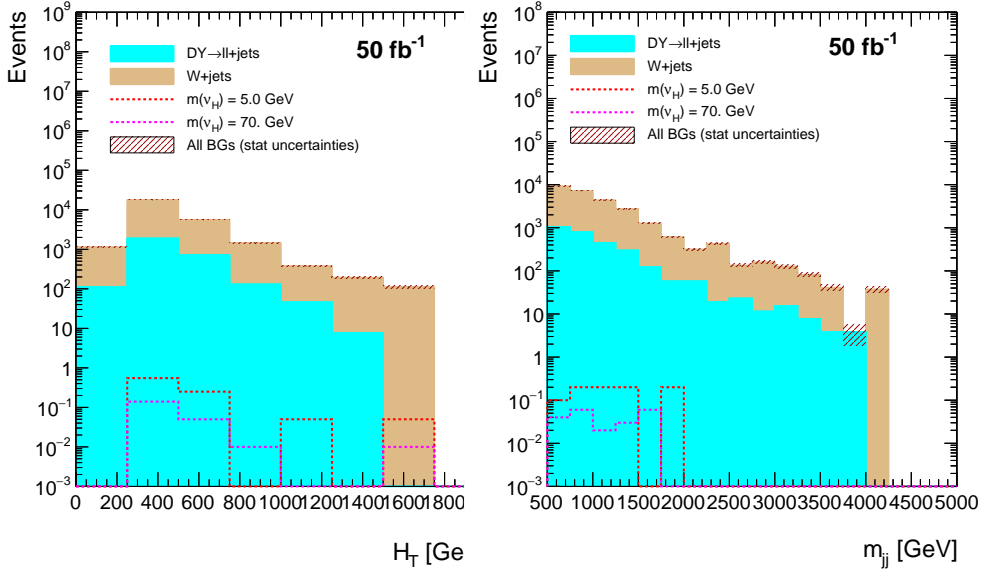


(a) H_T distribution for the signal and background (b) diJetMass distribution for the signal and background

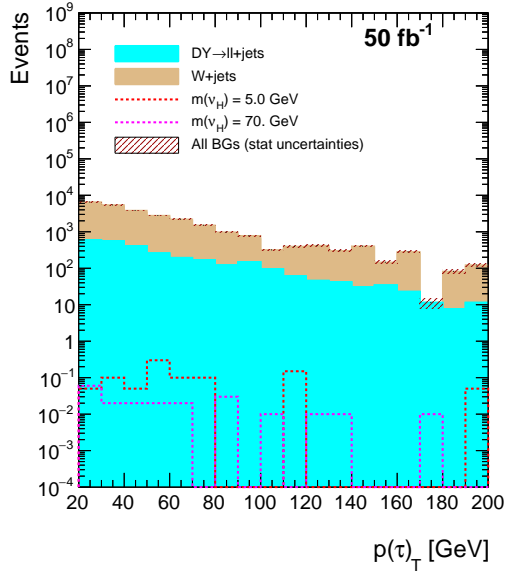


(c) $p_T(\tau)$ distribution for the signal and background

Figure 8.2: Distribution of different variables after cuts in the number of jets, taus and b-jets

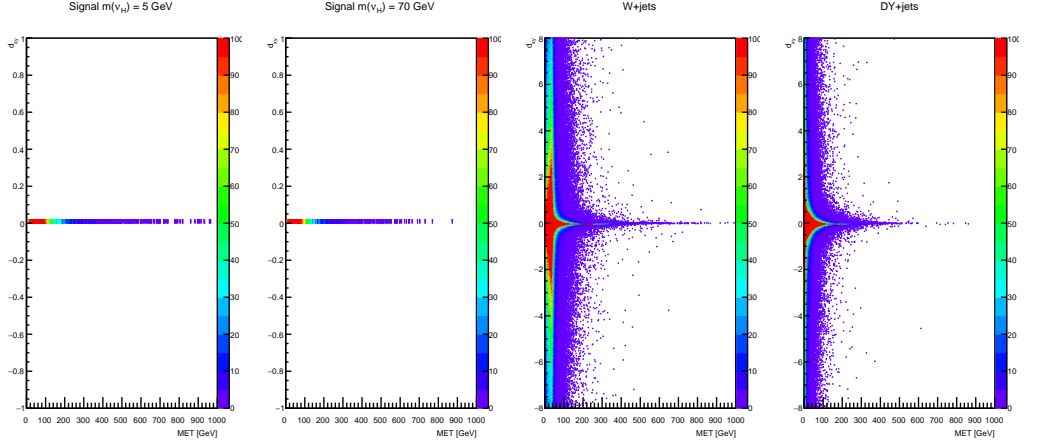
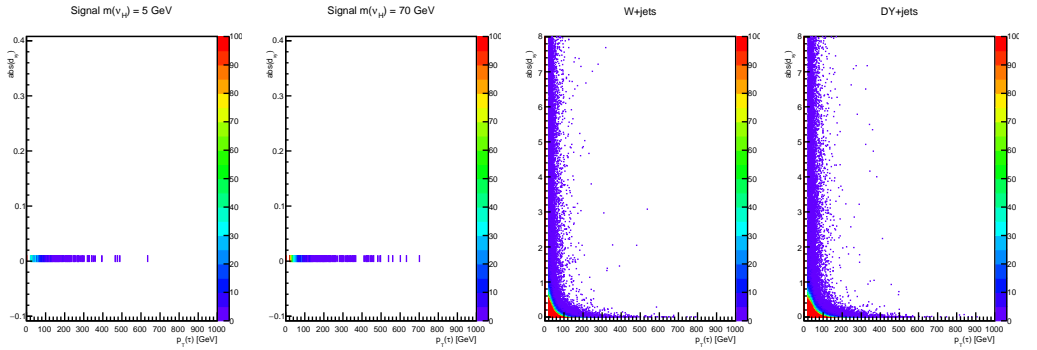


(a) H_T distribution for the signal and background (b) diJetMass distribution for the signal and background



(c) $p_T(\tau)$ distribution for the signal and background

Figure 8.3: Distribution of different variables after all the cuts

Figure 8.4: 2D graphic: E_T^{miss} vs d_{xy} Figure 8.5: 2D graphic: $p_T(\tau)$ vs $|d_{xy}|$ 

Chapter 9

Conclusions

The objective of this work was to perform a phenomenological analysis to determine a study that could reduce the backgrounds of our signal of interest under it. In order to do this, we started in Chapter 2 by making a brief summary of the SM and of what it states for neutrinos. Then, we studied the Majorana idea of writing the right-handed field in terms of the left-handed field. The former leads to the description of a Majorana mass term and the definition of a Majorana particle. Then, it is analyzed the Seesaw mechanism and the explanations it has for the mass of neutrinos are discussed. After, in Chapter 3 the relevant concepts and kinematical variables for this analysis were defined and explained.

In the chapter 4 the different parts of the CMS detector are described with the explanation of how they work and their characteristics. The CMS detector was explained with detail because in this analysis we considered events generated at this detector. Next, in chapter 5 the topology of the signals are explained: it is expected that the product tau has a displaced vertex, the presence of high energetic jets related to the VBF process, among other characteristics. The backgrounds of these signals were also explained with their final state characteristics. After, in the Chapter 6 the computational tools that were used in this analysis are described. It was mentioned each software and their specific task on the simulation of the signal or analysis of the data.

Then, the preselection criteria and the different cuts that were applied in this analysis were stated and explained in the Chapter 7. The following

Chapter 8 showed the analysis that was performed to study the signal and its background. It was showed that it was not possible to find optimal cuts in order to reduce the amount of background under the magnitude of the signal. The former was because, as it was shown, the kinematical and topological distributions of the signals and backgrounds were very similar. Additionally, the obtained the values of the impact parameter for the signals were unexpected, because they were very low and it was expected they had a large impact parameter value. The former can be a consequence that the size of the signal sample was small and that Delphes does not correctly reconstruct the secondary vertices.

Appendix A

Neutrinos and Seesaw Mechanism

First of all we are going to start by defining some fundamental concepts: helicity, quirality and projection operators. The helicity of a particle is defined as the projection of its spin onto the direction of its motion. It is said that a particle is right-handed when its spin is in the same direction as its motion and it is said a particle is left-handed when its spin is opposite in the opposite direction of its motion. In the case of massless particles the concept of quirality and helicity is equivalent. The quirality for a Dirac fermion is defined through the operator γ^5 with eigenvalues ± 1 . Thus a Dirac field can be projected into its left or right component by acting the operators P_R and P_L upon it. The right- and left-handed projection operators are defined as:

$$P_R = \frac{1 + \gamma^5}{2} \quad \text{and} \quad P_L = \frac{1 - \gamma^5}{2} \quad (\text{A.1})$$

A.0.1 Dirac Mass

In this Appendix we are going to perform with detail the calculations for neutrino physics which were mentioned in the State of the Art Chapter. We start here by studying the Dirac Mass, which is a term of the form:

$$m\bar{\psi}\psi = m(\overline{\psi_L + \psi_R})(\psi_L + \psi_R) = m(\overline{\psi_L}\psi_L + \overline{\psi_L}\psi_R + \overline{\psi_R}\psi_L + \overline{\psi_R}\psi_R) \quad (\text{A.2})$$

Lets study the term $\overline{\psi}_L \psi_L$ and using $P_R P_L = 0$:

$$\overline{\psi}_L \psi_L = \overline{\psi} P_L^\dagger P_L \psi = \overline{\psi} P_R P_L \psi = 0 \quad (\text{A.3})$$

Using an analogous reasoning we can find $\overline{\psi}_R \psi_R = 0$, too. Finally, we obtain the expresion:

$$m \overline{\psi} \psi = m (\overline{\psi}_L \psi_R + \overline{\psi}_R \psi_L) \quad (\text{A.4})$$

A.0.2 Majorana Mass

The expression we had for the Dirac Lagrangian was:

$$\begin{aligned} L &= \overline{\psi} (i \gamma^\mu \partial_\mu - m) \psi \\ &= (\overline{\psi}_L + \overline{\psi}_R) (i \gamma^\mu \partial_\mu - m) (\psi_L + \psi_R) \\ &= i \overline{\psi}_L \gamma^\mu \partial_\mu \psi_L + i \overline{\psi}_L \gamma^\mu \partial_\mu \psi_R - m \overline{\psi}_L \psi_L - m \overline{\psi}_L \psi_R \\ &\quad + i \overline{\psi}_R \gamma^\mu \partial_\mu \psi_L + i \overline{\psi}_R \gamma^\mu \partial_\mu \psi_R - m \overline{\psi}_R \psi_L - m \overline{\psi}_R \psi_R \end{aligned} \quad (\text{A.5})$$

We already proved that $\overline{\psi}_L \psi_L = \overline{\psi}_R \psi_R = 0$. Now we are going to study the second term in the Equation A.5, which has a term of the form:

$$\begin{aligned} P_R \gamma^\mu &= \frac{1}{2} (1 + \gamma^5) \gamma^\mu = \frac{1}{2} (\gamma^\mu + \gamma^5 \gamma^\mu) \\ &= \frac{1}{2} (\gamma^\mu - \gamma^\mu \gamma^5) \quad \text{Since } \{\gamma^5, \gamma^\mu\} = \gamma^5 \gamma^\mu + \gamma^\mu \gamma^5 = 0 \\ &= \frac{1}{2} \gamma^\mu (1 - \gamma^5) = \gamma^\mu P_L \end{aligned} \quad (\text{A.6})$$

Using what we have found in the last expression, we get for the second term:

$$\begin{aligned} i \overline{\psi}_L \gamma^\mu \partial_\mu \psi_R &= i \overline{\psi} P_R \gamma^\mu \partial_\mu P_R \psi \\ &= i \overline{\psi} \gamma^\mu P_L \partial_\mu P_R \psi \\ &= i \overline{\psi} \gamma^\mu \partial_\mu P_L P_R \psi \quad \text{Since } P_L \text{ is a constant operator} \\ &= 0 \end{aligned} \quad (\text{A.7})$$

Following a similar calculation we get: $i\overline{\psi_R}\gamma^\mu\partial_\mu\psi_L = 0$. Our next step is to find the two coupled Dirac equations using the Euler-Lagrange equation. We obtained for the Lagrangian:

$$L = i\overline{\psi_R}\gamma^\mu\partial_\mu\psi_R + i\overline{\psi_L}\gamma^\mu\partial_\mu\psi_L - m\overline{\psi_R}\psi_L - m\psi_L\psi_R \quad (\text{A.8})$$

Replacing in the Euler-Lagrange equation, we get for both states:

$$\begin{aligned} \frac{\partial L}{\partial(\partial\overline{\psi_R})} &= \frac{\partial L}{\partial\overline{\psi_R}} \rightarrow 0 = i\gamma^\mu\partial_\mu\psi_L - m\psi_R \\ \frac{\partial L}{\partial(\partial\overline{\psi_L})} &= \frac{\partial L}{\partial\overline{\psi_L}} \rightarrow 0 = i\gamma^\mu\partial_\mu\psi_R - m\psi_L \end{aligned} \quad (\text{A.9})$$

Now, we are going to find an expression for ψ_R in terms of ψ_L . First, we take the hermitian conjugate of the bottom equation in A.9:

$$\begin{aligned} i\gamma^\mu\partial_\mu\psi_R &= m\psi_L \\ (i\gamma^\mu\partial_\mu\psi_R)^\dagger &= m\psi_L^\dagger && \text{Taking the hermitian conjugate} \\ -i\partial_\mu\psi_R^\dagger\gamma^{\mu\dagger} &= m\psi_L^\dagger \\ -i\partial_\mu\psi_R^\dagger\gamma^{\mu\dagger}\gamma^0 &= m\psi_L^\dagger\gamma^0 && \text{Multiplying on the right by } \gamma^0 \\ -i\partial_\mu\psi_R^\dagger\gamma^0\gamma^\mu &= m\psi_L^\dagger\gamma^0 && \text{Using } \gamma^{\mu\dagger}\gamma^0 = \gamma^0\gamma^\mu \\ -i\partial_\mu\overline{\psi_R}\gamma^\mu &= m\overline{\psi_L} && \text{We have } \overline{\psi} = \psi^\dagger\gamma^0 \\ -i(\partial_\mu\overline{\psi_R}\gamma^\mu)^\top &= m\overline{\psi_L}^\top && \text{Taking the transpose} \\ -i\gamma^{\mu\top}\partial_\mu\overline{\psi_R}^\top &= m\overline{\psi_L}^\top \\ -i(-C^{-1}\gamma^\mu C)\partial_\mu\overline{\psi_R}^\top &= m\overline{\psi_L}^\top && \text{Using } \gamma^{\mu\top} = -C^{-1}\gamma^\mu C \\ i\gamma^\mu\partial_\mu C\overline{\psi_R}^\top &= mC\overline{\psi_L}^\top && \text{Multiplying on the left by } C \end{aligned} \quad (\text{A.10})$$

As we saw previously, for the lastest equation to have a similar structure as the top equation of A.9, the right-handed component of ψ must be:

$$\psi_R = C\overline{\psi_L}^\top \quad (\text{A.11})$$

Now, we need to prove that $C\overline{\psi}_L^\top$ is actually right-handed. To do this we apply the left-handed chiral projection operator P_L on this state and the result must be zero.

$$\begin{aligned} P_L \left(C\overline{\psi}_L^\top \right) &= CP_L^\top \overline{\psi}_L^\top \quad \text{Property of C: } P_L C = CP_L^\top \\ &= C \left(\overline{\psi}_L P_L \right)^\top \end{aligned} \quad (\text{A.12})$$

Now, let us examine the term $\overline{\psi}_L P_L$:

$$\begin{aligned} \overline{\psi}_L P_L &= (P_L \psi)^\dagger \gamma_0 P_L = \psi^\dagger P_L \gamma_0 P_L \\ &= \psi^\dagger \gamma^0 P_R P_L = 0 \end{aligned} \quad (\text{A.13})$$

Hence $C\overline{\psi}_L^\top$ is in fact a right-handed quiral state.

A.0.3 Seesaw Mechanism

Now, let us find the neutrino mass values by diagonalizing the matrix M :

$$M = \begin{pmatrix} m_L & m_D \\ m_D & m_R \end{pmatrix} \quad (\text{A.14})$$

In order to find the mass eigenvalues we need to solve the equation:

$$|M - I\lambda| = \left| \begin{pmatrix} m_L - \lambda & m_D \\ m_D & m_R - \lambda \end{pmatrix} \right| = 0 \quad (\text{A.15})$$

We obtain a quadratic equation of the form:

$$\lambda^2 - (m_L + m_R)\lambda + (m_L m_R - m_D^2) = 0 \quad (\text{A.16})$$

Using the quadratic equation to find the values of λ we get:

$$\begin{aligned} m_{1,2} &= \frac{(m_L + m_R) \pm \sqrt{(m_L + m_R)^2 - 4(m_L m_R - m_D^2)}}{2} \\ &= \frac{(m_L + m_R) \pm \sqrt{(m_L - m_R)^2 - 4m_D^2}}{2} \end{aligned} \quad (\text{A.17})$$

Now, setting $m_L = 0$ and assuming $m_R \gg m_D$, we obtain the following mass eigenstates. For the neutrino field ν_1 the mass is given by Equation A.18, and for the neutrino field ν_2 the mass is give by the Equation A.19.

$$m_1 = \frac{m_D^2}{m_R} \quad (\text{A.18})$$

$$m_2 = m_R \left(1 + \frac{m_D^2}{m_R^2} \right) \approx m_R \quad (\text{A.19})$$

Bibliography

- [1] Gonzalez-Garcia, M., Maltoni, M., & Schwetz, T. (2016). Global analyses of neutrino oscillation experiments. *Nuclear Physics B*, 908, 199-217. <http://dx.doi.org/10.1016/j.nuclphysb.2016.02.0331>
- [2] Balantekin, A. & Haxton, W. (2013). Neutrino oscillations. *Progress In Particle And Nuclear Physics*, 71, 150-161. <http://dx.doi.org/10.1016/j.pnpnp.2013.03.007>
- [3] Bhupal, P.S., Mohapatra, R.N., and Zhang, Y. (2016). Heavy right-handed neutrino dark matter in left-right models. Retrieved from <https://arxiv.org/abs/1610.05738>
- [4] Bhupal, P.S., Mohapatra, R.N., and Zhang, Y. (2016). Naturally Stable Right-Handed Neutrino Dark Matter. Retrieved from <https://arxiv.org/abs/1608.06266>
- [5] Almeida Jr., F., Coutinho, Y., Martins Simões, J., Vale, M., & Wulck, S. (2001). Dirac and Majorana heavy neutrinos at LEP II. *The European Physical Journal C*, 22(2), 277-281. <http://dx.doi.org/10.1007/s100520100798>
- [6] Gluza, J., Jelinsky, T. (2015). Heavy neutrinos and the $pp \rightarrow l\bar{l}jj$ CMS data. Retrieved from <http://www.sciencedirect.com/science/article/pii/S0370269315005080>
- [7] Aad, G., Abbott, B., Abdallah, J., Abdel Khalek, S., Abidinov, O., & Aben, R. et al. (2015). Search for heavy Majorana neutrinos with the ATLAS detector in pp collisions at $s = 8 \sqrt{s} = 8$ TeV. *Journal Of High Energy Physics*, 2015(7). [http://dx.doi.org/10.1007/jhep07\(2015\)162](http://dx.doi.org/10.1007/jhep07(2015)162)

- [8] Gago, A., Hernández, P., Jones-Peréz, J., Losada, M., Moreno, A. (2015). Probing the Type I Seesaw Mechanism with Displaced Vertices at the LHC. Retrieved from <https://arxiv.org/abs/1505.05880v2>
- [9] Molinaro, E. (2013). Type I Seesaw Mechanism, Lepton Flavour Violation and Higgs Decays. Retrieved from <https://arxiv.org/pdf/1303.5856v1.pdf>
- [10] Neutrino Mass and Direct Measurements. (2015) (1st ed.). Retrieved from https://www2.warwick.ac.uk/fac/sci/physics/staff/academic/boyd/stuff/lec_neutrinomass_writeup.pdf
- [11] Kim, C., & Pevsner, A. (1993). Neutrinos in physics and astrophysics (1st ed.). Langhorne, PA: Harwood Academic.
- [12] Grupen, C., Shwartz, B., & Spieler, H. (2011). Particle detectors (1st ed.). Cambridge: Cambridge University Press.
- [13] Kirschenmann, H. (2017). Sketch of pp-collision and resulting collimated spray of particles, a jet. Retrieved from <https://phys.org/news/2012-07-jets-cms-energy-scale.html>
- [14] HUERTAS, L. (2016). Estudio fenomenológico de búsquedas de nueva física en el LHC, mediante la producción de pares de staus en conjunto con un jet de ISR. (Master of Science). Universidad de los Andes.
- [15] Fruhwirth, R., & Regler, M. (2000). Data Analysis Techniques for High-energy Physics (Cambridge Monographs on Particle Physics, Nuclear Physics, and Cosmology) (1st ed.). Cambridge University Press.
- [16] Schott, M. (2017). Illustration of the ATLAS and CMS coordinate system. Retrieved from <https://inspirehep.net/record/1294662/plots>
- [17] Azuma, Y. SUSY searches with Displaced Vertices (Disappearing Tracks) in ATLAS. Lecture, Berkeley.
- [18] DORNEY, B. (2017). Visualization of the Impact Parameter (IP, red line) of a track (Image courtesy of Jean-Roch Vlimant, of the CMS Collaboration). Retrieved from

- <http://www.quantumdiaries.org/2011/06/10/to-b-or-not-to-bbar-b-tagging-via-track-counting/>
- [19] CMS. (2011). Detector overview. Retrieved from <http://cms.web.cern.ch/news/detector-overview>
 - [20] Kane, G., & Pierce, A. (2008). Perspectives on LHC physics (1st ed.). Singapore [u.a.]: World Scientific.
 - [21] Muon Drift Tubes — CMS Experiment. (2017). Cms.web.cern.ch. Retrieved 17 May 2017, from <http://cms.web.cern.ch/news/muon-drift-tubes>
 - [22] Cathode Strip Chambers — CMS Experiment. (2017). Cms.web.cern.ch. Retrieved 17 May 2017, from <http://cms.web.cern.ch/news/cathode-strip-chambers>
 - [23] Resistive Plate Chambers — CMS Experiment. (2017). Cms.web.cern.ch. Retrieved 17 May 2017, from <http://cms.web.cern.ch/news/resistive-plate-chambers>
 - [24] LHC collisions. (2017). Lhc-machine-outreach.web.cern.ch. Retrieved 17 May 2017, from <https://lhc-machine-outreach.web.cern.ch/lhc-machine-outreach/collisions.htm>
 - [25] Dutta, B., Gurrola, A., Johns, W., Kamon, T., Sheldon, P., & Sinha, K. (2013). Vector boson fusion processes as a probe of supersymmetric electroweak sectors at the LHC. *Physical Review D*, 87(3). <http://dx.doi.org/10.1103/physrevd.87.035029>
 - [26] Alwall, J., Herquet, M., Maltoni, F., Mattelaer, O., & Stelzer, T. (2011). MadGraph 5: going beyond. *Journal Of High Energy Physics*, 2011(6). [http://dx.doi.org/10.1007/jhep06\(2011\)128](http://dx.doi.org/10.1007/jhep06(2011)128)
 - [27] Alwall, J., Frederix, R., Frixione, S., Hirschi, V., Maltoni, F., & Matelaer, O. et al. (2014). The automated computation of tree-level and next-to-leading order differential cross sections, and their matching to parton shower simulations. *Journal Of High Energy Physics*, 2014(7). [http://dx.doi.org/10.1007/jhep07\(2014\)079](http://dx.doi.org/10.1007/jhep07(2014)079)

- [28] Sjöstrand, T., Ask, S., Christiansen, J., Corke, R., Desai, N., & Ilten, P. et al. (2015). An introduction to PYTHIA 8.2. *Computer Physics Communications*, 191, 159-177. <http://dx.doi.org/10.1016/j.cpc.2015.01.024>
- [29] de Favereau, J., Delaere, C., Demin, P., Giammanco, A., Lemaître, V., Mertens, A., & Selvaggi, M. (2014). DELPHES 3: a modular framework for fast simulation of a generic collider experiment. *Journal Of High Energy Physics*, 2014(2). [http://dx.doi.org/10.1007/jhep02\(2014\)057](http://dx.doi.org/10.1007/jhep02(2014)057)
- [30] Antcheva, I., Ballintijn, M., Bellenot, B., Biskup, M., Brun, R., & Buncic, N. et al. (2009). ROOT — A C++ framework for petabyte data storage, statistical analysis and visualization. *Computer Physics Communications*, 180(12), 2499-2512. <http://dx.doi.org/10.1016/j.cpc.2009.08.005>